X-ray beam induced current/microprobe x-ray fluorescence: synchrotron radiation based x-ray microprobe techniques for analysis of the recombination activity and chemical nature of metal impurities in silicon

2004 J. Phys.: Condens. Matter 16 S141

(http://iopscience.iop.org/0953-8984/16/2/017)

INSTITUTE OF PHYSICS PUBLISHING JOURNAL OF PHYSICS: CONDENSED MATTER

J. Phys.: Condens. Matter **16** (2004) S141–S151 PII: S0953-8984(04)66921-9

X-ray beam induced current/microprobe x-ray fluorescence: synchrotron radiation based x-ray microprobe techniques for analysis of the recombination activity and chemical nature of metal impurities in silicon

O F Vyvenko[1], T Buonassisi[2], A A Istratov[2] and E R Weber[3]

[1] V A Fok Institute of Physics, St Petersburg State University, 198504 St Petersburg, Petrodvoretz, Uljanovskaja 1, Russia
[2] University of California, LBNL, MS62R0203, 1 Cyclotron Road, Berkeley, CA 94720, USA
[3] University of California, Department of Materials Science and Engineering, 374 Hearst Mining Boulevard, Berkeley, CA 94720, USA

E-mail: vyvenko@paloma.spbu.ru

Received 31 July 2003
Published 22 December 2003
Online at stacks.iop.org/JPhysCM/16/S141 (DOI: 10.1088/0953-8984/16/2/017)

Abstract

In this study we report applications of the synchrotron radiation based x-ray microprobe techniques, x-ray beam induced current (XBIC) and microprobe x-ray fluorescence (μ-XRF), to the analysis of the recombination activity and spatial distribution of transition metals in silicon. A combination of these two techniques enables one to study the elemental nature of defects and impurities and their recombination activity *in situ* and to map metal clusters with a micron-scale resolution. The correspondence between XBIC data and the data obtained by conventional recombination-sensitive mapping techniques such as electron beam induced current and laser beam induced current is demonstrated. An approach that allows determination of the depth of metal precipitates from several XBIC/μ-XRF images taken for different sample orientations is suggested and is experimentally demonstrated.

1. Introduction

Transition metals are more detrimental for silicon device yield than any other impurity [1, 2]. Due to their high diffusivity and solubility in silicon, they easily penetrate from the wafer surface into the bulk during any heat treatment. The strong temperature dependence of the equilibrium solubilities of the metals causes their supersaturation during cooling, which results in the formation of metal precipitates or complexes. These precipitates are usually found in the vicinity of structural defects such as grain boundaries or dislocations.

Lattice positions and electronic properties of the dissolved transition metal impurities, e.g., iron, copper, and nickel, are now well established. In contrast to this, reports on the properties of metal precipitates or metal-decorated extended defects such as dislocations are scant and contradictory. The metal precipitates formed intentionally by diffusing metals into high purity silicon and quenching the samples to room temperature were found to form deep electronic states near the middle of the bandgap [3–5], thus providing an effective channel for minority carrier recombination and generation. Recombination active metal precipitates were also found in as-grown multicrystalline silicon which was not intentionally contaminated and mc-Si solar cells [6]. The energy distribution of the electronic states associated with metal precipitates was found to be dependent on the precipitate morphology [4]. However, there are no systematic data on the dependence of the morphology of the precipitates on their recombination properties. The existing indirect [7] and direct [8, 9] data indicate that the recombination activity of metal precipitates in silicon can vary between very strong and very weak.

In order to improve our understanding of the recombination activity of metal precipitates, one has to collect data on both their recombination activity and their non-electrical properties such as their elemental composition and morphology. Until recently, the only tool which was available for *in situ* studies of the recombination activity and chemical nature of the precipitates was electron beam induced current (EBIC) combined with the energy dispersive spectroscopy (EDS) mode of scanning electron microscopy (SEM). However, the detection limit of electron beam excited x-rays is too low (about 0.1–1 at.%) to detect most metal precipitates due to a high background of bremsstrahlung.

The use of high brightness synchrotron radiation to probe defects in silicon allows one to circumvent the problem of a high bremsstrahlung background plaguing electron beam based techniques and increases the sensitivity of the x-ray fluorescence and absorption techniques to the level where they can be used to characterize small metal clusters in silicon. It was shown [10, 11] that beamline 10.3.1 at the Advanced Light Source (synchrotron facility) at the Lawrence Berkeley National Laboratory can be used to detect iron and copper in silicon with a 1–2 μm spatial resolution at concentrations that are at least two orders of magnitude lower than the detection limit of the EDS-SEM technique. Moreover, the microprobe x-ray fluorescence (μ-XRF) technique (beamline 10.3.1) can be complemented by the x-ray absorption spectromicroscopy (μ-XAS) technique (Beamline 10.3.2) that allows one to determine the chemical composition of precipitates of the same small sizes [10].

In the past, the samples used for XRF analyses were usually pre-characterized with EBIC or laser beam induced current (LBIC) in order to find the areas of low minority carrier diffusion length which could subsequently be mapped at the XRF beamline. However, a direct correlation between recombination activity of a defect and its chemical nature was generally very difficult to achieve since it was almost impossible to match the maps obtained by independent μ-XRF and lifetime measurement techniques with an accuracy on the order of a micron. Recently, we suggested a novel lifetime-sensitive technique, x-ray beam induced current (XBIC) [8]. The XBIC signal, which carries information about the minority carrier lifetime, can be measured simultaneously with the x-ray fluorescence (μ-XRF) signal, which characterizes the chemical nature of the sample excited by the beam, including, e.g., impurity precipitates. This combination enabled us to study the chemical nature of the defects and impurities and their recombination activity *in situ* and to map metal clusters with a micron-scale resolution.

In this paper we give a review of our recent work dealing with the application of XBIC/μ-XRF to the analysis of the recombination activity and spatial distribution of transition metal in silicon structures and silicon solar cells, and suggest a new experimental procedure

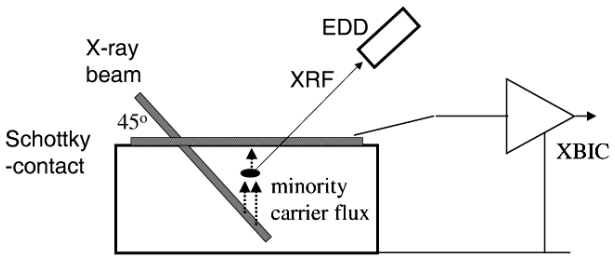

Figure 1. A schematic diagram of the XBIC/XRF experiment. The focused x-ray beam from a synchrotron is incident at an angle of 45° to the sample surface. X-ray fluorescence arising when the beam hits the metal precipitate is measured by a Si:Li energy dispersive detector (EDD). Minority carriers induced due to absorption of x-ray photons are collected with a Schottky diode. A reduction of the minority carrier diode current due to enhanced recombination at a defect gives rise to the appearance of the XBIC contrast.

which allows one to determine depth of the metal precipitates from XBIC/μ-XRF maps taken for different sample orientations.

2. X-ray fluorescence and x-ray beam induced current techniques

A diagram of the XBIC/μ-XRF experiment is shown in the figure 1. An intense x-ray beam from the synchrotron with approximately 3×10^{10} photons s^{-1} is focused in a (1–2) $\times$ (1.5–3) μm^2 spot using elliptically bent multilayer mirrors. The incident x-ray beam has a wide range of photon energies with a peak of intensity at 12.4 keV. The beam hits the sample surface at an angle of 45°. The emanating x-ray fluorescence is detected by a Si:Li detector with an energy resolution of about 180 eV. The penetration depth of the incoming x-rays is large, about 180 μm in silicon (at the incident angle of 45°). However, the sampling depth of the XRF technique (26 μm for iron and 50 μm for copper) is determined mostly by the extinction length of the fluorescence x-rays of interest, that increases with the atomic number, Z. The sensitivity of the XRF tool depends on the accumulation time, t_a, at each point, which can be chosen rather long due to a low background signal of the XRF experiment ($1/10$ photons s^{-1}), on the mass-absorption coefficient of the element at the exciting x-ray beam energy, and on its fluorescence yield. For $t_a = 30$ s, a single iron precipitate with a radius of 20–25 nm, or dissolved iron or copper at concentrations of about 10^{14} and 7×10^{14} cm^{-2} respectively, can be detected [10]. The absolute values of the impurity concentration are determined using a calibration with XRF standards.

The principle of XBIC is similar to EBIC or LBIC, with the only difference that minority charge carriers, generated by an electron beam in EBIC or laser beam in LBIC, are generated in XBIC by a focused x-ray beam. The electron beam or x-ray beam is scanned across the surface and the current collected with the Schottky diode or p–n junction is measured to form an image of the electrically active defects. Due to the large attenuation depth of the exciting radiation, XBIC sampling depth is determined primarily by the diffusion length of excess minority carriers in most practical cases. Additionally, the inclined beam orientation leads to a shift of XBIC image with respect to μ-XRF in the direction of the beam projection on the sample surface. This is because the maximum in XRF yield is achieved when the x-ray beam hits the precipitate, whereas the minimum in XBIC current is reached when the x-ray beam goes below the precipitate, so that the generated carriers can get trapped and recombine on their way to the p–n junction. The excitation level of the XBIC experiments is similar

to a low excitation regime of EBIC. Indeed, the focused x-ray beam photon flux of about 10^{10} photons s^{-1} with an energy of 12.4 keV generates the same number of electron–hole pairs in silicon as an electron current of about 1 nA with the same energy. However, the absorbed energy is spread over a 250 μm x-ray propagation path (note that the penetration depth of 180 μm mentioned above is calculated along the sample normal), which is roughly 50 times greater than the projected range of electrons with the same energy. Hence, the excitation conditions of an XBIC experiment corresponds to approximately 20 pA electron beam excitation, i.e., a current which is considered a low excitation regime in EBIC. This allowed us to quantitatively compare contrast of defects in EBIC and XBIC images, see below.

XBIC/μ-XRF studies were performed either on fully processed solar cells with p–n^+ junctions or on chemically cleaned semiconducting wafers. In the latter case 20 nm thick Pd or Au Schottky contacts were thermally evaporated on the surface of the sample and Ohmic contacts were formed by rubbing gallium at the edges of the sample on its back surface. A 20 nm layer of Pd or Au on top of the sample neither significantly absorbed the x-rays, nor affected the penetration depth of the x-ray beam or the sensitivity of the μ-XRF technique.

No external bias was applied to the contact; the built-in voltage of the Schottky diode was used to collect the charge carriers. All measurements were performed in air at ambient pressure. The air ionization/fluorescence excited with the intense x-ray beam gave rise to a background XBIC signal (increased with the contact area increase) which was compensated in the current amplifier by subtracting a current offset.

The sample was mounted in an XRF sample holder, which can be moved in the X and Y directions with a minimum step size of 0.1 μm by computer-controlled stepper motors. Both μ-XRF and XBIC signals were measured simultaneously and were stored in a computer as a function of the (X, Y) coordinates of the sample stage. These data could be later retrieved to plot the maps of minority carrier lifetime and metal impurity distribution, or to perform data analyses at any point within the scan.

The use of XBIC in combination with μ-XRF offers several advantages, including

(a) the interesting area of the sample found by conventional recombination sensitive methods (EBIC, LBIC) can be easily located in an XBIC map for the subsequent detailed analysis with XRF;
(b) correspondence between XBIC and EBIC/LBIC builds a bridge to the direct comparison of XRF data with the results of other scanning methods (cathodoluminescence, optical luminescence mapping, lock-in thermography, photoacoustic spectroscopy etc), and
(c) XBIC enables one to establish a direct relation between recombination activity of a defect and concentration of metals at this location.

3. Examples of XBIC/μ-XRF application

The first example of the application of the XBIC/μ-XRF technique demonstrates correlation of XBIC with the conventional lifetime mapping techniques such as EBIC. A comparison of EBIC and XBIC scans, taken on the same contact of the mc-Si sample, is shown in figures 2(a) and (b) (left-hand column). Both scans cover the area of approximately 3 mm $\times$ 1.7 mm. There is a clear correlation between the maps obtained by both techniques. However, the contrast of individual defects may be different in EBIC and XBIC maps depending on their depth from the surface. This is because the typical penetration depth of the impinging electron beam in the EBIC technique is less than 10 μm, whereas in XBIC the detection depth is determined by the smallest of the minority carrier diffusion length or of the penetration depth of the x-ray beam. Since the solar cell collection efficiency is determined in part by the minority carrier diffusion

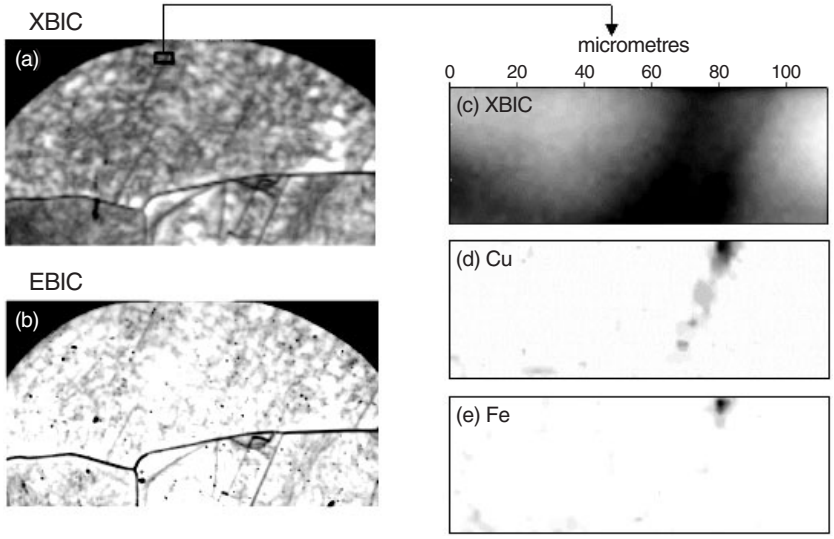

Figure 2. Left: comparison of the XBIC (a) and EBIC (b) of the same area of an mc-Si sample. The correlation between the minority carrier diffusion length maps obtained by both techniques is obvious. Right: XBIC (c) and μ-XRF maps of the Cu (d) and Fe (e) distributions of the area marked with the black rectangle on the large-scale XBIC map (a). XBIC contrast is assumed to be due to a group of dislocations parallel to the sample surface. Both Kα and Kβ peaks were observed for Cu and Fe, thus confirming their correct identification. 112 μm $\times$ 40 μm area scan.

length of the semiconductor under investigation, XBIC is a better tool to detect lifetime limiting defects that may affect the solar cell performance than EBIC. On the other hand, the lateral resolution of XBIC is lower than that of EBIC. This limitation is mostly due to the x-ray beam angle of incidence of 45° and the larger penetration depth of the x-ray beam. The resolution limit of XBIC, estimated from our data, is comparable to that of LBIC (which, for longer wavelengths, has a carrier generation depth similar to XBIC) and is on the order of 10 μm. For comparison, with EBIC one can obtain resolutions at or below 1 μm.

Figures 2(c)–(e) (right-hand column) show XBIC and μ-XRF iron and copper distribution maps for a small area marked on the large overview XBIC map on the left-hand side of the figure. All three maps were recorded simultaneously. A weak contrast of an extended defect, possibly of a group of dislocations going parallel to the surface, is visible in the XBIC map, figure 2(c). μ-XRF maps of the same area, presented in figures 2(d) and (e), revealed clusters of the aforementioned transition metals precipitated at these defects. It is interesting to note that despite a fairly high metal concentration in the clusters, their apparent recombination activity is quite low, judged by the weak XBIC contrast. This can either indicate that the detected metal clusters lie at a significant depth from the wafer surface, so that only a small fraction of minority carriers generated at that depth can diffuse to the Schottky diode, or by a low electrical activity of these precipitates.

In our previous publications, we also demonstrated good agreement between lifetime features detected in XBIC and LBIC maps [8, 12, 13]. It was found that XBIC maps coincide well with LBIC maps when the penetration depths of the excitation radiations are comparable. Since LBIC can be readily used to map large area fully processed solar cells, one can use XBIC/LBIC combination as a bridge to correlate μ-XRF maps of transition metals with lock-in thermography maps [14] with sufficient accuracy in order to determine metal content at the

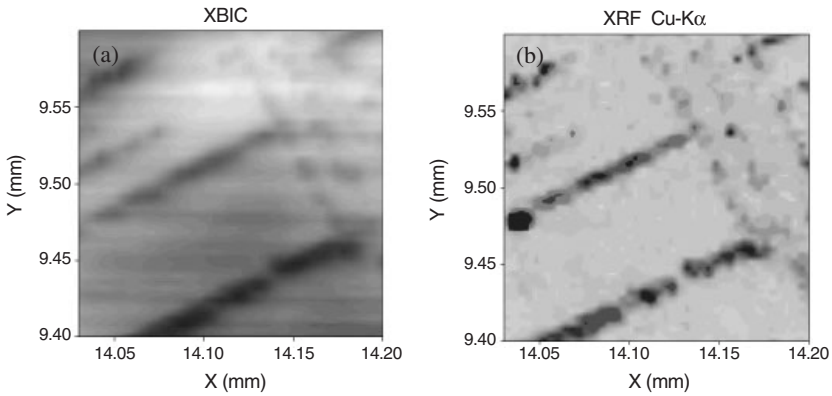

Figure 3. XBIC (left) and μ-XRF map of the Cu Kα intensity distribution (right) of an area of a copper-doped Si–$Si_{0.98}Ge_{0.02}$ structure with misfit dislocations. Dark XBIC regions correspond to a reduction of the diode current whereas the dark Cu Kα regions correspond to increased copper concentration. A good correlation between the recombination activity and the copper concentration distribution is obvious.

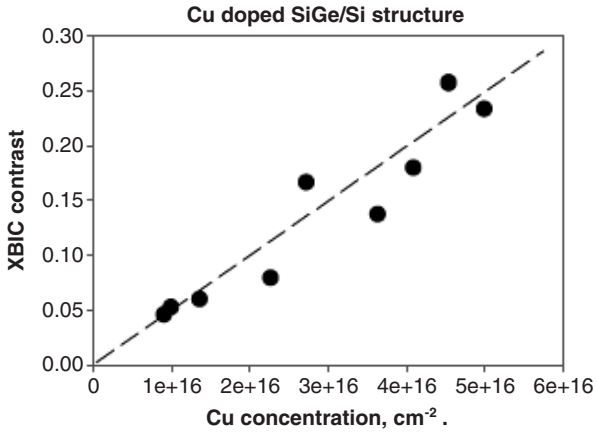

Figure 4. XBIC contrast versus XRF copper concentration as derived from the maps in figure 3 along the horizontal axis. A linear dependence of the XBIC contrast on Cu concentration is evident.

shunt locations. Indeed, it was found that some types of shunt contain transition metals, which may be partially or fully responsible for the formation of these shunts.

The next example, presented in figures 3 and 4, demonstrates how the XBIC/μ-XRF data can be used to obtain a quantitative relation between the concentration of transition metals precipitated at an extended defect and the recombination activity of these precipitates. We investigated SiGe/Si structures with a concentration of shallow donors of 10^{15} cm^{-3} consisting of a 2 μm thick $Si_{0.98}Ge_{0.02}$ layer sandwiched between a 2.5 μm silicon bottom buffer layer grown on a (001) n^+ silicon substrate and a 2.5 μm thick silicon cap layer grown by chemical-vapour deposition (CVD). A network of two perpendicular sets of 60° misfit dislocations running in the ⟨110⟩ directions was observed at the interfaces between Si and $Si_{0.98}Ge_{0.02}$. The samples were intentionally contaminated with iron or copper. Further details of the sample preparation and other results obtained on those samples, e.g., by EBIC, can be

found elsewhere [9, 15, 16]. Since dislocations are confined to the interfaces between Si and $Si_{0.98}Ge_{0.02}$, any influence of the defect depth distribution on results is excluded.

XBIC and XRF Cu Kα maps of a SiGe/Si structure doped with copper are shown in figures 3(a) and (b) respectively. Dark areas on the XBIC map correspond to a reduction of the diode current whereas the dark regions in the Cu Kα map correspond to an increased copper concentration. One can see that the dark contrasts in both images are grouped in two sets of mutually perpendicular straight lines corresponding to two sets of misfit dislocations. Individual copper precipitates can be distinguished in many parts of the XRF image. There is clearly a good correlation between the recombination activity and the copper concentration distributions; i.e., the higher the intensity of the copper related x-ray fluorescence, the lower the XBIC current. In figure 4 the XBIC contrast is plotted against the copper concentration per cm^{-2}, N_s, determined from the raw XRF data calibrated by using an XRF standard.

To compare our μ-XRF results on the copper concentration with the previously published data, we estimated an average thickness of the precipitates in the direction perpendicular to the sample surface from the absolute copper concentration determined from the XRF data assuming that they consist of copper silicide, Cu_3Si. Using the value for the atomic density of Cu in Cu_3Si of $\rho = 6 \times 10^{22}$ cm^{-3} [17], the apparent thickness of the precipitates, $d_{XRF} = N_s/\rho$, observed in figure 3 was calculated to vary between 1.6 and 10 nm. These values are close to the minimum thickness of Cu_3Si platelet-like precipitates found from TEM measurements for rapidly quenched samples [5]. This implies that the precipitates at dislocations in our samples either indeed consist of overlapping or nearly overlapping very thin platelets, or consist of thicker precipitates of smaller sizes which do not overlap with each other. The latter assumption seems to be more likely since it is in correspondence with TEM results on dislocation-free silicon [18, 19] showing the copper silicide precipitates of nanometre sizes grouped in dense colonies.

The XBIC contrast was calculated as the ratio $\Delta I/I_0$, where $\Delta I = (I_0 - I_d)$, I_0 is the XBIC current value far away from the defect, and I_d is the value of the XBIC current at the location of the precipitate. The maximum XBIC contrast value observed in our samples was around 30%, whereas the EBIC contrast of similar samples was up to 70% [9, 16]. Since the excitation levels of EBIC and XBIC are fairly close to each other, we believe that this discrepancy is due to a smaller fraction of the total current collected by the precipitates in the XBIC measurements than in EBIC measurements.

The dependence shown in figure 4 can be well approximated with a straight line. An exact theory of the XBIC contrast with the particular generation function of the XBIC experiment has not yet been developed. Nonetheless, we can interpret the observed dependence by using the particular properties of the investigated structure. A close inspection of the XBIC/XRF maps in figure 3 shows that the lateral size of the metal-related recombination-active precipitate appears to exceed the total thickness of the structure and the x-ray beam diameter. Taking into account that the minority carrier lifetime in the n^+ substrate is expected to be very low due to Auger recombination, the main contribution to XBIC signal must originate from the electron–hole pairs generated within the near-surface $Si/Si_{0.98}Ge_{0.02}/Si$ structure. In this case, only the minority carriers which are generated in the structure just beneath the misfit dislocation planes and diffused to the contact will contribute to XBIC contrast, i.e., the dimensions of the effective generation volume are of about the thickness of the structure beneath the misfit dislocation plane ($\sim$5 μm). Hence, lateral diffusion of the minority carriers in the vicinity of a defect of a larger lateral size can be neglected and the continuity equation can be written as $\Delta I_z/\Delta z = -R$, where I_z is the minority carrier current to the contact, R is the recombination rate per unit volume within the layer containing precipitates, and Δz is its thickness [20]. The equation together with the proportional dependence of XBIC contrast on the copper density

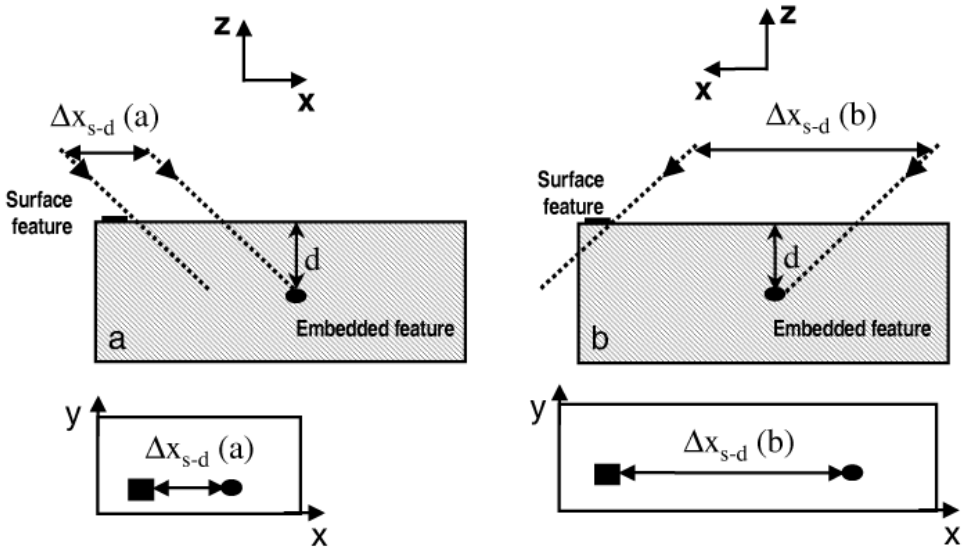

Figure 5. A schematic diagram explaining defect depth determination by using two subsequent XBIC/μ-XRF scans performed before (a) and after (b) 180° sample rotation around the z-axis, perpendicular to the sample surface. The direction of the x-ray beam with respect to the sample of scan a (b) is depicted with dotted straight lines. The depth d of the object of interest (*embedded feature*) and its true distance Δx_{true} on x-scale with respect to a *surface feature* (reference) are calculated by the expressions $d = (\Delta x_{\text{s}-\text{d}}(\text{b}) - \Delta x_{\text{s}-\text{d}}(\text{a}))/2$, $\Delta x_{\text{true}} = (\Delta x_{\text{s}-\text{d}}(\text{b}) + \Delta x_{\text{s}-\text{d}}(\text{a}))/2$, where $\Delta x_{\text{s}-\text{d}}(\text{a})$ and $\Delta x_{\text{s}-\text{d}}(\text{b})$ are the apparent distances between the image of the object and the image of the *surface feature* (reference) obtained on the XBIC/μ-XRF maps of scans a and b respectively.

per unit area of the sample surface, N_{Cu} (cm^{-2}), implies that N_{Cu} (cm^{-2}) is proportional to $-R\Delta x$, or that R is proportional to N_{Cu} (cm^{-3}), the average copper volume density.

The proportionality of the recombination rate and the total number of metal atoms in any given precipitate can be explained assuming that all (or the same fixed percentage of) metal atoms in all precipitates are (is) electrically active. Such an assumption is in concordance with the conclusion made from the analysis of DLTS data [5, 21].

4. XBIC/μ-XRF depth determination (3D mapping)

EBIC/LBIC techniques allow one to determine the depth of a defect by using variation of the penetration depth of the exciting beam, i.e., by variation of accelerating voltage or wavelength of the exciting light beam. Unfortunately, this approach cannot be used to determine the depth of a defect with the XBIC/μ-XRF technique since beamline 10.3.1 uses incoming x-rays with the energies determined by the parameters of the synchrotron and the mirrors used in the set-up. This is why we developed another approach to determine the depth of defects from the surface by taking advantage of the geometry of the experimental set-up at beamline 10.3.1. We utilized the fact that the focused synchrotron x-ray beam is incident at a 45° angle to the sample.

A schematic diagram depicted in figure 5 explains the depth determination method of the defect by using two subsequent XBIC/μ-XRF mappings of the area of the sample with the defect of interest before and after 180° sample rotation around the axis perpendicular to the

wafer surface. In the coordinate system of the sample, the 180° rotation is equivalent to the change of the directions of the incident beam with respect to the sample as shown by the dotted lines in figures 5(a) and (b). In this way, the apparent position of the image of a defect relative to the surface features of the sample on the XBIC or μ-XRF map will change as schematically depicted at the bottom of figure 5. The depth **z** of the object of interest in the bulk of the sample as well as its true coordinate along the x-axis can be calculated as the half-difference and half-sum of the x-distances of the object relative to the surface mark before and after rotation, respectively (see also the figure 5 caption). In theory, one could perform full 3D imaging by taking a sequence of measurements at different sample rotation angles. However, to determine the depth of the defect it is sufficient to measure the distance changes of the apparent defect image in only two sample orientations, before and after 180° sample rotation with respect to a surface feature that exists already or can be prepared intentionally by evaporating a metal dot on the sample surface. The maximum depth that can be measured with this method is defined by the attenuation depth of the exciting x-ray beam (in our case, 180 μm), the minority carrier diffusion length in XBIC mapping (typically 30–100 μm) and, in the μ-XRF mapping, by the attenuation depth of the fluorescent radiation (typically 20–50 μm depending on the element). The accuracy of the method is defined by the spot size of the focused beam, by the scan step size, and by the sharpness of the surface reference and the defect image.

Figure 6 presents an example of the depth determination experiment performed on a fully processed silicon solar cell made from prototype RGS material (ribbon grown on substrate). Under certain growth conditions in RGS material, oxygen is known to precipitate at extended crystallographic defects, causing the formation of channels of inverse conductivity type. These channels may efficiently collect minority carriers from a greater depth of the substrate than the average minority carrier diffusion length when they extend from the emitter into the bulk. Current collecting channels can be identified in bevelled EBIC maps as bright spots [22]. The existence of the collecting channels explains a relatively high current collection efficiency of this type of solar cell material despite a very low minority carrier diffusion length.

The left-hand column in figure 6 represents XRF intensity maps of the silver Lα_1 fluorescence peak (2.984 keV). Silver is the main component of the contact strips. The Ag Lα fluorescence has an extinction depth in silicon as small as 3 μm and therefore could be used as a surface mark. Two images in the middle column of figure 6 represent the XBIC contrasts of the collecting channels as they appear before and after a 180° rotation of the sample. The positions of the contact strip edges are redrawn from the silver map on the XBIC maps as dashed lines. A shift of the current collecting channel to the right relative to the strip position and noticeable changes of the collecting channel image shape after the rotation are obvious. An area marked with sharp arrows shifts to the right by approximately 80 μm, whereas the area marked with the round-end arrow shifts by approximately 150 μm. These values imply that the conducting channel goes down from the right to the left from the depth of 40 μm to the depth of 75 μm.

The right-hand side column represents the XRF intensity map of the titanium Kα line. Titanium is a minor component of the contact strips that can be recognized in the images. Additionally, two titanium dots marked with dark arrows are seen in the images. The position of the lower dot with respect to the contact strip does not change after the rotation of the sample, indicating that it is a titanium particle on the sample surface. The upper titanium dot image shifted after the rotation by 20 μm to the right and overlaps with the contact strip. Due to a strong absorption of the Ti Kα radiation (4.5 keV) by silver in the contact strip the XRF contrast of the dot became weaker after the rotation. The shift corresponds to the defect depth of 10 μm and its true position on the x-scale in the middle between the position seen in the upper map and the contact strip.

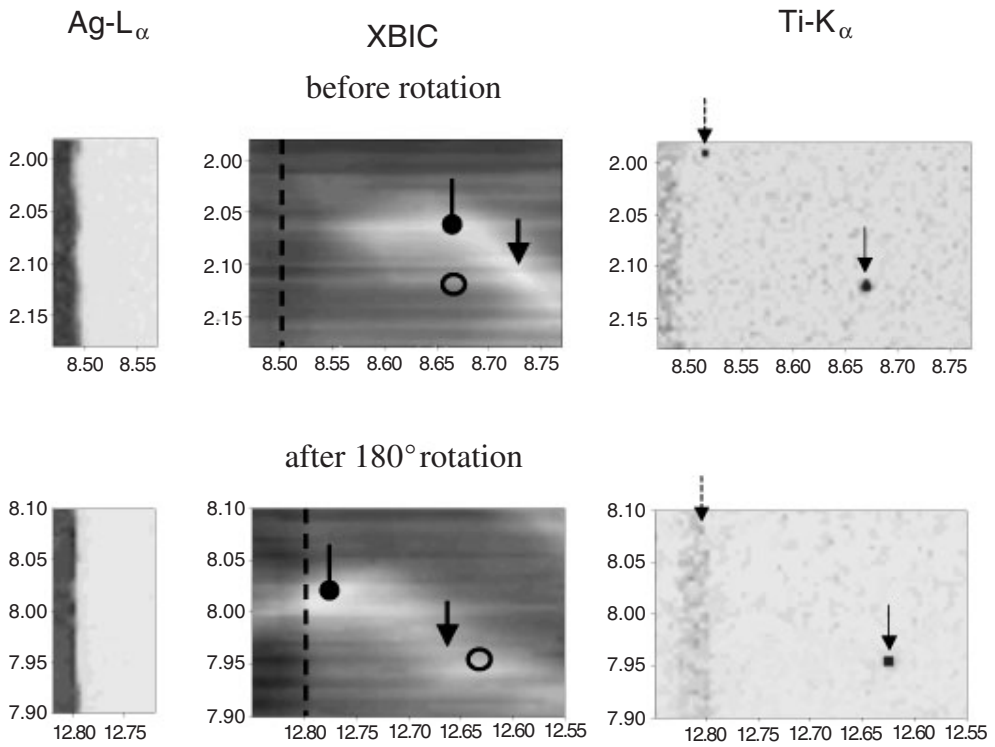

Figure 6. Determination of depth of current collecting channels in prototype RGS silicon by an XBIC/μ-XRF 180° rotation experiment. The top and bottom rows of images are taken before and after the rotation of the sample by 180° around the axis perpendicular to the sample surface. The bright XBIC contrast which images the shape of the current collecting channels changes after sample rotation (middle image column). Left- and right-hand image columns are μ-XRF silver and titanium maps, respectively, which were used as surface reference features. All three maps in every row were measured in a single scan. Note, the directions of the horizontal and vertical axes in the bottom row of the images are opposite to those in the top row.

5. Summary

In summary, an analytical tool capable of *in situ* measurements of the recombination activity of defects and their chemical origin has been demonstrated in application to the studies of mc-silicon, copper decorated misfit dislocations, and fully processed silicon solar cells. It has been shown that the XBIC/μXRF technique enables one to

- establish the direct relation between local metal concentration and recombination activity of the precipitates;
- rapidly locate the area of interest established by conventional recombination sensitive methods (EBIC, LBIC) for the subsequent detailed measurements with XRF;
- estimate the depth of the defects.

The correlation between XBIC, EBIC, and LBIC techniques builds a bridge to the direct comparison of XRF data with the results obtained with other scanning methods.

Acknowledgments

The funding for this research was provided by NREL, subcontract AAT-2-31605-03, and by the AG-Solar project of the government of Northrhein–Westfalia (NRW). The Advanced Light Source operations are funded by the Director, Office of Energy Research, Office of Basic Energy Sciences, Materials Sciences Division, of the US Department of Energy under Contract No. DE-AC03-76SF00098. The authors gratefully acknowledge fruitful discussions with M Kittler, W Seifert, A Thompson, S A McHugo, H Hieslmair, G D Ackermann, R Ynzunza, Z Hussein, R Schindler, and G Hahn.

References

[1] Istratov A A, Hieslmair H and Weber E R 2000 *Appl. Phys.* A **70** 489–534
[2] Istratov A A and Weber E R 1998 *Appl. Phys.* A **66** 123–36
[3] Riedel F, Kronewitz J, Gnauert U, Seibt M and Schroter W 1996 *Solid State Phenom.* **47/48** 359–64
[4] Riedel F and Schroter W 2000 *Phys. Rev.* B **62** 7150–6
[5] Istratov A A, Hedemann H, Seibt M, Vyvenko O F, Schröter W, Heiser T, Flink C, Hieslmair H and Weber E R 1998 *J. Electrochem. Soc.* **145** 3889–98
[6] McHugo S A, Thompson A C, Perichaud I and Martinuzzi S 1998 *Appl. Phys. Lett.* **72** 3482–4
[7] Istratov A A, Buonassisi T, McDonald R J, Smith A R, Rand J A, Kalejs J and Weber E R 2003 *J. Appl. Phys.* at press
[8] Vyvenko O F, Buonassisi T, Istratov A A, Hieslmair H, Thompson A C, Schindler R and Weber E R 2002 *J. Appl. Phys.* **91** 3614–7
[9] Vyvenko O F, Buonassisi T, Istratov A A, Weber E R, Kittler M and Seifert W 2002 *J. Phys.: Condens. Matter* **14** 13079–86
[10] McHugo S A, Thompson A C, Flink C, Weber E R, Lamble G, Gunion B, MacDowell A, Celestre R, Padmore H A and Hussain Z 2000 *J. Cryst. Growth* **210** 395–400
[11] McHugo S A, Thompson A C, Mohammed A, Lamble G, Perichaud I, Martinuzzi S, Werner M, Rinio M, Koch W, Hoefs H U and Haessler C 2001 *J. Appl. Phys.* **89** 4282–8
[12] Buonassisi T, Vyvenko O F, Istratov A A, Weber E R and Schindler R 2002 *MRS Proc.* **719** F6-6
[13] Buonassisi T, Vyvenko O F, Istratov A A, Weber E R, Hahn G, Geiger P, Rakotoniaina J P and Breitenstein O 2003 *J. Appl. Phys.* at press
[14] Breitenstein O, Iwig K and Konovalov I 1997 *Phys. Status Solidi* a **160** 271–82
[15] Higgs V and Kittler M 1993 *Appl. Phys. Lett.* **63** 2085–7
[16] Kittler M, Ulhaq-Bouillet C and Higgs V 1995 *J. Appl. Phys.* **78** 4573–83
[17] Ronay M and Schad R G 1990 *Phys. Rev. Lett.* **64** 2042–5
[18] Nes E and Lunde G 1972 *J. Appl. Phys.* **43** 1835–9
[19] Seibt M and Graff K 1988 *J. Appl. Phys.* **63** 4444–50
[20] Orton J W and Blood P 1990 The Electrical Characterization of Semiconductors: Measurement of Minority Carrier Properties *Techniques of Physics* vol 13, ed N H March (London: Academic)
[21] Kveder V, Kittler M and Schroter W 2001 *Phys. Rev.* B **63** 115208/1–11
[22] Breitenstein O, Langenkamp M and Rakotoniaina J P 2001 *Solid State Phenom.* **78/79** 29–37